IX International Conference on Computational Methods in Marine Engineering
MARINE 2021
I.M. Viola and F. Brennan (Eds)

COMPUTATIONAL PREDICTION OF PROPELLER CAVITATION NOISE

MILTIADIS KALIKATZARAKIS*, ANDREA CORADDU*, MEHMET ATLAR*, GIORGIO TANI†, STEFANO GAGGERO†, DIEGO VILLA†, AND LUCA ONETO⋆

*Naval Architecture, Ocean & Marine Engineering
University of Strathclyde
100 Montorse Street, G4 0LZ, Glasgow, UK
e-mail: miltiadis.kalikatzarakis@strath.ac.uk; andrea.coraddu@strath.ac.uk;
mehmet.atlar@strath.ac.uk

†DITEN, Polytechnic School
University of Genoa
Via Montallegro 1, 16145, Genoa, Italy
e-mail: giorgio.tani@unige.it; stefano.gaggero@unige.it; diego.villa@unige.it

⋆DIBRIS
University of Genova
Via Opera Pia 11a, I-16145 Genova, Italy
e-mail: luca.oneto@unige.it

Key words: Cavitation Noise, Controllable Pitch Propeller

Abstract. The potential impact of ships underwater radiated noise (URN) on marine fauna has become an important issue. The most dominant noise source on a propeller-driven vessel is propeller cavitation, and the accurate prediction of its noise signature is fundamental for the design process. In this work, we investigate the potential of using low-computational-cost methods for the prediction of URN from cavitating marine propellers that can be conveniently implemented within the design process. We compare computational and experimental results on a subset of the Meridian standard propeller series, behind different severities of axial wake, for a total of 432 experiments.

1 INTRODUCTION

Underwater Radiated Noise (URN) is a subject of increased interest in naval architecture primarily because of its negative consequences on marine life and, secondly, considerations about the comfort of crew and passengers. The propeller is the most significant noise source, generating the highest noise levels at frequencies below 200 Hz. While the understanding of various noise generation mechanisms is still an ongoing area of research, the development of different methods to accurately predict ship-generated noise becomes more important and imminent. Unfortunately, the effect of cavitation and its dynamics on URN is complex, and the current state of the art does not offer a plausible physically-based URN prediction method that can be conveniently implemented within the propeller design procedure.

In this work, we evaluate the potential of utilising a Boundary Element Method (BEM) to predict the pressure distribution on the surface of the propeller blades, and the semi-empirical methods of [1, 2] to estimate the broadband effects of sheet cavitation, and the radiated noise due to tip vortex cavitation, respectively. Computational results are compared with experiments performed on a small, but commercially representative, subset of the Meridian standard series propeller models. These were tested in the Emerson Cavitation Tunnel, behind different severities of the axial wake created using three two-dimensional wake screens. A total of 432 unique combinations of propeller model and inflow conditions are investigated.

The rest of the paper is organised as follows. Section 2 presents the set of computational methods used to evaluate flow features and the URN for the considered propellers and wake fields. Section 3 details the experimental data used to evaluate the accuracy of the proposed methods. Section 4 discusses the process of estimating the parameters of the methods described in Section 2. Section 5 reports comparative results between the numerical methods and the experimental data, and Section 6 collects some conclusions of the paper.

2 NUMERICAL METHODS

In this section we give a brief overview of the numerical methods employed to compute the URN spectra that will be compared with experimental measurements in Section 5.

2.1 Boundary Element Method

We performed unsteady hydrodynamic computations by means of an in-house developed Boundary Element Method (BEM) that provides an accurate characterisation of the hydrodynamic field of the propeller at an acceptable computational cost [3]. The BEM models the flow field around a solid body using a scalar function being the perturbation potential ϕ, whose spatial derivatives represent the perturbation potential velocity vector component. Assuming irrotationality, incompressibility, and the absence of viscosity allows to express the continuity equation as a Laplace equation for the perturbation potential as $\nabla^2\phi(\boldsymbol{x}, t) = 0$.

Green's third identity allows to solve the three dimensional differential problem as a simpler integral problem written for the surfaces that bound the domain. In the context of non-cavitating flows, these surfaces include the fully wetted surface of the blades (S_B) and of the hub (S_H) plus the trailing wake surface S_W. The latter refers to the zero thickness layer, which departs at the trailing edge of the lifting surfaces, where vorticity is shed onto the downstream flow, as shown in Figure 1. The solution is obtained as the intensity of a series of mathematical singularities distributed on the boundaries (i.e. dipoles $-\phi$ and sources $\frac{\partial\phi}{\partial n}$) which superposition models the inviscid flow in the entire computational domain [4]:

$$2\pi\phi\left(\tilde{\boldsymbol{x}}, t\right) = \int_{S_B+S_H} \phi\left(\boldsymbol{x}, t\right) \frac{\partial}{\partial \boldsymbol{n}} \frac{1}{\boldsymbol{r}} dS - \int_{S_B+S_H} \frac{\partial\phi(\boldsymbol{x}, t)}{\partial \boldsymbol{n}} \frac{1}{\boldsymbol{r}} dS + \int_{S_W} \Delta\phi_{\text{wake}}\left(\boldsymbol{x}, t\right) \frac{\partial}{\partial \boldsymbol{n}} \frac{1}{\boldsymbol{r}} dS \quad (1)$$

where $\boldsymbol{n}$ is the unit normal, $\boldsymbol{r}$ is the distance between points $\tilde{\boldsymbol{x}}$ and $\boldsymbol{x}$, and Δ denotes the potential jump (i.e. the net dipole intensity) across the wake surface. The pressure forces, once the potentials are defined, can be computed by applying the unsteady formulation of Bernoulli's theorem.

The numerical solution consists of an inner iterative scheme that solves the non-linearities related to the Kutta condition at the blade trailing edge and an outer iterative cycle to integrate over time by shedding in the wake the correct amount of vorticity in accordance with the Kelvin theorem. To this aim, the *key-blade* approach proposed by [5] is exploited: only one blade (plus its wake and portion of the hub) is solved while the influence of other blades is accounted iteratively during propeller revolutions until a periodic solution after the numerical transient is achieved. In current analyses we use a surface mesh for the *key-blade* of 1000 panels plus 360 on the hub. The trailing vortical wake extends for eight revolutions with a spatial discretization corresponding to an equivalent time step of 6 deg.

2.2 Broadband Effects of Sheet Cavitation

To estimate the noise induced by sheet cavitation we adopt the method of [1], summarised in this Section. The sheet cavitation is the typical cavitation bubble shape that occurs when a lifting profile experienced a significant angle of attack. Due to the low-pressure values occurring on the leading edge profile portion, a cavitation bubble (with the shape of a sheet) grows from the leading edge towards trailing edge until the pressure exceeds the vapour limit destroying it. Consequently, attached sheet cavitation on a propeller blade initiates and grows while an upcoming propeller blade enters into the wake peak. After the sheet cavity reaches its maximum volume, it starts to retreat, a process that is associated with parts of the cavity breaking off into bubble clouds. In [1] it is assumed that the volume rate of the generated bubbles equals the rate at which the sheet cavity volume decreases:

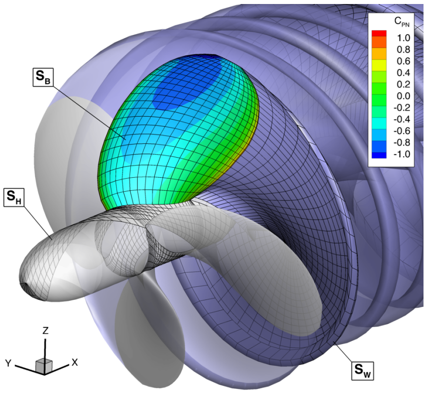

Figure 1: Mesh arrangement on the propeller surface and resulting pressure coefficient. KCD 192 in steady flow, $J = 0.6$.

$$\begin{cases} \dfrac{\partial}{\partial t}\left(\displaystyle\sum_{i=1}^{n_c} V_i\right) = \dfrac{\partial}{\partial t}\left(n_c \bar{V}\right) = -\beta \dfrac{\partial}{\partial t}\left(A_c\right) dr, & \text{for } \dfrac{\partial}{\partial t}\left(A_c\right) < 0 \\ \dfrac{\partial}{\partial t}\left(\displaystyle\sum_{i=1}^{n_c} V_i\right) = \dfrac{\partial}{\partial t}\left(n_c \bar{V}\right) = 0 & \text{for } \dfrac{\partial}{\partial t}\left(A_c\right) \geq 0 \end{cases} \tag{2}$$

where V_i is the volume on the i-th bubble, with the total number of bubbles for one time-step being n_c. A_c is the cavitating area in a cross section of the blade, and it estimated using the method of [6] using as input the unsteady pressure distributions computed with the Boundary Element Method. β refers to the gas / vapour fraction, assumed equal to 0.8 in [1], and ∂r is the blade span differential.

The average bubble volume $\bar{V}$ is defined on the basis of the size distribution of the bubbles,

Table 1: Constants of Gilmore equation [8].

Parameter	Symbol	Value [1]	Units	Parameter	Symbol	Value [1]	Units
Polytropic index	k	1.4	[-]	Bulk constant	B	3×10^8	[Pa]
Bulk constant	n	7	[-]	Vapour pressure	p_v	857	[Pa]
Initial gas pressure	p_{g0}	857	[Pa]	Surface Tension	S	0.0725	[N/m]

which is assumed to be a beta distribution, as

$$f_v(x) = \frac{m}{4\pi} \frac{(1-x)^{m-1}}{x^2}, \; x = \frac{2R}{C\frac{A_c}{L_c}} \tag{3}$$

in which m is a constant, assumed equal to 0.9 in [1], and x is the non-dimensional bubble radius. R is the bubble radius, L_c is the cavity length, and C is a constant having the value of 1.8 in [1]. Assuming that the mean value of the bubble volume remains constant within one time-step (Δt), the total number of bubbles (Δn_c) generated in one time-step for blade length (dr) is

$$\Delta n_c = -\frac{\beta}{\bar{V}} \left(A_c(t + \Delta t) - A_c(t) \right) \partial r \tag{4}$$

The newly-generated bubbles Δn_c are transported towards the trailing edge at the local speed of the flow U, and blade pressure is assumed to increase monotonically from the vapour pressure p_v, to the static pressure p_0 at the trailing edge. Under the assumption of linear pressure growth, the ambient pressure at the location of the bubble can be approximated as

$$p_\infty(t) = p_v + \frac{t}{t^*}(p_0 - p_v) \tag{5}$$

with $t^* = (c - L_c)/U$ being the bubble travelling time to the trailing edge, and c being the local sound velocity.

The computations are performed for every time-step (Δ_t), and for all radial sections of the key blade. If the local cavity is shrinking, i.e. a bubble cloud is generated, the total number of cavitation bubbles and their mean volume are evaluated and discretized into a number of bubble classes N_c, assumed equal to 5 in [1]. To compute the pressure trace generated by each bubble class, a bubble dynamics equation must be integrated over time. Several approaches can be utilised to describe the oscillations of radially symmetric bubbles, e.g the equations of Rayleigh-Plesset, Gilmore, Keller - Miksis and Flynn [7]. Here we have employed the Gilmore equation, which is solved for a fixed number of oscillations τ_c, equal to 3.5 in [1], who further suggests that the time-traces obtained are offset by a random, uniformly distributed, time lag within the current time-step, with the assumption that the initial gas pressure in the bubble is equal to the vapour pressure. The constants used in the Gilmore equation are given in Table 1.

This procedure is applied to every bubble in each bubble class and for all classes, with the summation of all time traces forming the total field pressure.

2.3 Tip Vortex Induced Noise

To estimate the URN due to tip vortex cavitation, we used the Empirical cavitating Tip Vortex (ETV) model [2]. ETV is a semi-empirical model, based on the Tip Vortex Index (TVI) method [9]. TVI relates measured inboard noise levels, to the predicted size of the vortex cavity using a computed circulation distribution on the propeller blade determined by a potential flow method. The ETV model follows a similar approach, but with the difference that it predicts the broadband spectrum of URN slightly differently.

The authors utilised the Proctor vortex model [10] for the distribution of the azimuthal velocity with radius, given by

$$v_\theta(r) = \begin{cases} 1.0939\dfrac{\Gamma_\infty}{2\pi r}\left(1 - exp\left(-b\left(\dfrac{1.4r_v}{D/2}\right)^p\right)\right)\left(1 - exp\left(-\zeta\left(\dfrac{r}{r_v}\right)^2\right)\right) & \text{for } r \leq 1.4r_v \\ \dfrac{\Gamma_\infty}{2\pi r}\left(1 - exp\left(-b\left(\dfrac{r}{D/2}\right)^p\right)\right) & \text{for } r > 1.4r_v \end{cases} \tag{6}$$

where r_v is the size of the viscous core, and D is the propeller diameter. Γ_∞ is the vortex strength for the tip blade section (here considered at $r/R = 0.95$), computed by the BEM method of Section 2.1, and averaged over one complete propeller revolution. c_1 and b have to be estimated through a curve-fitting procedure, and $\zeta = 1.2564, p = 0.75$ as suggested in [11]. Regarding the size of the viscous core, reference values from [12] have been used, scaled according to the procedure proposed in [13], to account for the different Reynolds numbers.

With the known azimuthal velocity distribution, the pressure distribution can be obtained, by integrating the momentum equation in the radial direction. This process relates the cavity size with the cavitation number, from which the cavity size can be estimated. Subsequently, it is used to estimate the source level spectrum, which is divided in two frequency parts: the part that is characterised by a hump around the resonance frequency of the vortex cavity f_c, due to the overall growth, collapse and rebounds of the cavity, $(H_h(f))$, and the part related to the final phase of the cavity collapse process, which consists of prescribed slopes at frequencies much lower and much higher than the resonance frequency $(H_s(f))$, given by

$$H_h(s) = 20log_{10}\left(sinc\left(\frac{f - f_c}{0.83\Delta f_{-6dB}}\right)\right),\ H_s(s) = 10log_{10}\left(\frac{2(f/f_c)^{a_l}}{1 + (f/f_c)^{a_l - a_h}}\right) \tag{7}$$

where Δf_{-6dB} is the bandwidth of the hump for which the pressure amplitude is equal to half the maximum, a_h is the slope of the high-frequency, and a_l is the slope of the low-frequency. Typical values, as suggested in [14], are $a_l = 4, a_h = -2$.

The resonance frequency of the vortex f_c is derived based on theoretical considerations and with the use of the experimental data of [15], as

$$f_c = \frac{0.45\pi^2\sigma_{tip}nZ}{\tau K_t} \tag{8}$$

where K_t is the propeller's thrust coefficient, Z the number of propeller blades, n the rotational speed, τ is an unknown parameter obtained through curve fitting on the experimental data, and σ_{tip} is the cavitation index based on the resultant velocity at the blade tip.

The source level spectrum is thus modelled as a weighted sum of the two spectral functions H_h and H_s

$$SL(f) = L_{p,max} + 10log_{10}(\alpha 10^{H_h(f)/10} + (1 - \alpha)10^{H_s(f)/10}) \tag{9}$$

where α is a user-defined parameter, and $L_{p,max}$ is the maximum level of the hump of the power density spectrum, given by

$$L_{p,max} = a_p + 20log_{10}\left(\left(\frac{\tau r_c}{D}\right)^{k_p}\sqrt{Z}\right) \tag{10}$$

with a_p and k_p being empirical constants, to be estimated from experimental data. In [9] $k_p = 2$ is suggested, however in [2] the value $k = 3$ was reported to provide more accurate results, as such the same has been utilised in this work.

3 EXPERIMENTAL DATA DESCRIPTION

In order to benchmark the methods described in Section 2, we utilised the large dataset developed in [16]. The authors performed an extensive measurement campaign by conducting systematic cavitation tunnel tests at the Emerson Cavitation Tunnel of Newcastle University, with 6 members of the Meridian Standard propeller series and three variations of the wake inflow conditions. Based on these propellers and wake inflow conditions, the authors conducted a full factorial experimental design, including three different levels of tunnel vacuum conditions (atmospheric, 150 mmHg, 300 mmHg) and eight propeller rotational speeds, with a constant inflow velocity of 3 m/s, resulting in 432 experiments.

For the sake of completeness, we give a description of the wake inflows in Section 3.1 and an overview of the propeller models in Section 3.2. A more detailed discussion of the experimental setup and measurements can be found in [16].

3.1 Wakefields

In [16] suitable wake configurations were selected, based on the criteria suggested by [17]. According to these studies, wakefields with steeper velocity changes produce higher tonal amplitudes of pressure fluctuations, as well as high-frequency contributions from increased dynamic cavity collapses, both on and away from the blade surface. Based on these observations, the wake non-uniformity, mean wake, half- wake width and wake depth were controlled, in order to generate three wakefields that would induce variation in the inflow velocities of varying severity. These changes would then induce the formation of unsteady cavitation from the collapse and rebound of cavity volumes at the exit of the wake peak region. The generated wakefields are shown in Figure 2.

3.2 Propellers

The Meridian propeller series, derived from the proprietary propeller design of Stone Manganese Marine Ltd., is a unique standard series based solely on practical propeller designs for standardised variations in pitch-to-diameter ratio (P/D), blade area ratio (A_E/A_O) and number of blades. Initially, the series comprised four parent models having a combination of four distinct blade area ratios $A_E/A_O \in \{0.45, 0.65, 0.85, 1.05\}$, and five mean pitch-to-diameter ratios $P/D \in \{0.4, 0.6, 0.8, 1.0, 1.2\}$. All the propellers had a diameter of 304.8 mm and 6 blades, with a boss diameter $r_h = 0.185 \times D/2$. Currently there are 60 propellers in the series, with $Z \in \{4, 5, 6\}$, $A_E/A_O \in (0.45-1.05)$ and $P/D \in (0.4-1.2)$. A visual impression of the propellers is presented in Figure 3.

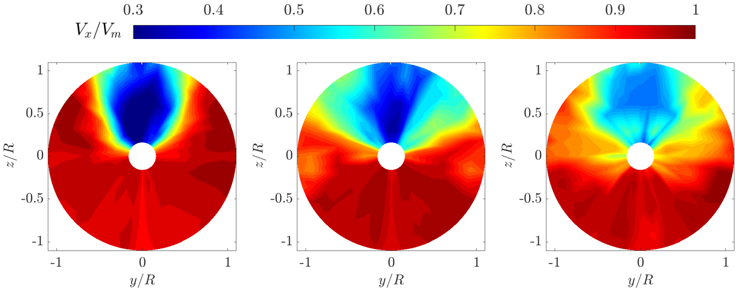

(b) W1 (c) W2 (d) W3

Figure 2: Contour plots of axial velocity distributions of the wakefields in the dataset.

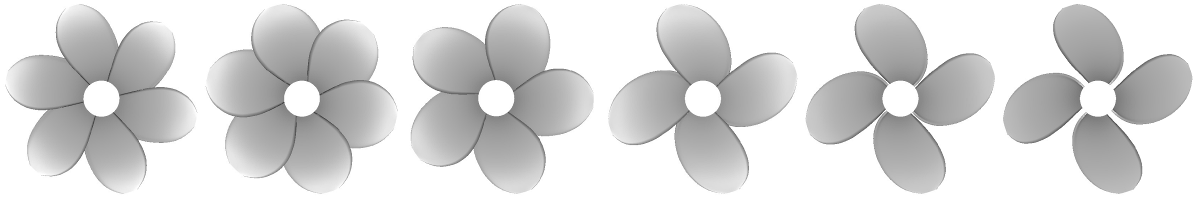

(a) KCD 65 (b) KCD 74 (c) KCD 129 (d) KCD 191 (e) KCD 192 (f) KCD 193

Figure 3: Visual impression of the propellers in the dataset.

4 PARAMETER ESTIMATION

Having computed the pressure distribution on the propeller surface with the BEM code of Section 2.1, we can estimate the URN by the combination of the models discussed in Sections 2.2 - 2.3 for any given experiment, by providing the appropriate parameter values required by both models.

4.1 Parameter Overview

As discussed in Sections 2.2 - 2.3, both models have a set of parameters whose values arise either from theoretical considerations, or through a fitting process on experimental data. In Table 2 we present an overview of the parameters used in the methods of Sections 2.2 - 2.3.

Table 2: Parameters of Sections 2.2 - 2.3.

Method	Symbol	Equation	Value*	Method	Symbol	Equation	Value*
Matusiak Model (Section 2.2)	β	Eq. (2)	0.8	ETV Model (Section 2.3)	b, c_1	Eq. (6)	-
	m, C	Eq. (3)	9, 1.8		Δf_{-6dB}, a_l, a_h	Eq. (7)	-, 4, -2
	τ_c	-	1.8		τ	Eq. (8)	-
	N_c	-	5		α	Eq. (9)	0.8
					a_p, k_p	Eq. (10)	-, 3

* [-] indicates that no default value exists, thus a curve-fitting procedure must be used.

The method employed for the prediction of URN from sheet cavitation (Section 2.2) requires the estimation of 5 parameters. The author in [1] performed a detailed calibration study and thoroughly discussed the choice of certain parameter values, along with their physical interpretation. However, the calibration process was performed using limited measurements and certain parameter values were chosen for reasons of computational cost that do not apply anymore. For these reasons, certain parameters were chosen for re-estimation directly from the experimental data, in order to enhance the predictive capabilities of the method.

Note that Table 2 excludes the constants employed in the Gilmore equation, shown in Table 1. We expect non-negligible differences by altering the values of these constants, e.g. by modifying the value for the polytropic index k, which determines if the process is adiabatic ($k = 1.4$) or isothermal ($k = 1$). Moreover, the assumption that the initial gas pressure p_{g0} is equal to the vapour pressure can be refined by actually computing p_{g0}, on the basis of the initial (undisturbed) pressure outside the bubble, following a suggestion mentioned in [7], and implemented in [18]. Nevertheless, their values have been kept constant in this work, along with the original assumption made in [1]. Regarding the ETV model of Section 2.3, 9 parameters have to be estimated. The author of [2] has performed an extensive analysis on several datasets in the past, both in model-scale and full-scale data, under a variety of operating conditions. Nevertheless, the nature of the method requires the implementation of a fitting process in order to improve predictions.

4.2 Problem Formulation

The parameter estimation process can be formulated as an optimisation problem, with the decision variables being the values of the necessary parameters, and the objective (cost) function being an error metric that quantifies the different between the actual and the predicted URN spectra. Formally, we seek the solution to the following continuous, non-convex problem

$$\begin{aligned} \arg\min_{\boldsymbol{\theta}} \qquad & \hat{L}(\boldsymbol{\theta}) = \sum_{i=1}^{M} l(h(\boldsymbol{X}_i, \boldsymbol{\theta}), \boldsymbol{y}_i) = \sum_{i=1}^{M} (h(\boldsymbol{X}_i, \boldsymbol{\theta}) - \boldsymbol{y}_i)^2 \\ \text{subject to:} \qquad & \boldsymbol{\theta}_{min} \leq \boldsymbol{\theta} \leq \boldsymbol{\theta}_{max} \end{aligned} \tag{11}$$

where $\boldsymbol{\theta} \in \Theta^{14}$ is the set of parameters according to Section 4.1 that need to be estimated from a given bounded space Θ^{14}, and $\hat{L}(\theta, \mathscr{D}_M)$ is the empirical error of the physical model h on the dataset $\mathscr{D}_M = \{(\boldsymbol{X}_1, \boldsymbol{y}_1), (\boldsymbol{X}_2, \boldsymbol{y}_2), ..., (\boldsymbol{X}_M, \boldsymbol{y}_M)\}$, measured according to a loss function $l(h(\boldsymbol{X}, \boldsymbol{\theta}), \boldsymbol{y})$. As can be seen from Eq. (11), for the latter we have adopted the square loss. $\boldsymbol{X}$ denotes the model inputs, i.e. the propeller geometry, wakefield and inflow conditions, and the pressure distribution on the key-blade for one complete revolution, and $\boldsymbol{y} \in \mathbb{R}^p$ refers to the measured radiated noise levels at different frequencies that characterise the entire URN spectrum. Because $\boldsymbol{y}$ is a vector, we have re-defined the loss function as the average absolute difference between the actual and predicted URN spectra. This is permitted since they both represent homogeneous quantities, and the average difference between the two can describe the quality of h in a satisfactory manner.

4.3 Performance Metrics

It is important to note that the experimental data needs to be split into two different subsets, to objectively evaluate the performance of h. The set $\mathscr{D}_M$ that is used to tune the parameters of h by solving Problem (11), and the set $\mathscr{T}_K = \{(\boldsymbol{X}^t_1, y^t_1), (\boldsymbol{X}^t_2, y^t_2), ..., (\boldsymbol{X}^t_K, y^t_K)\}$ to evaluate (test) the performance of h on a real-world scenario. These subsets have been created by splitting randomly the experimental data, keeping 70% of the data in $\mathscr{D}_M$, and 30% of the data in $\mathscr{T}_K$. Note that $\mathscr{T}_K$ is required since the error that h would commit over $\mathscr{D}_M$ would be too optimistically biased since it has been used to estimate h itself.

For this reason, additional performance metrics are reported in Section 5 that refer only to the performance of h on $\mathscr{T}_K$, in order to provide a complete description of the quality of the model. With $h(\boldsymbol{X}, \boldsymbol{\theta})$ referring to the outputs of the model arising from the solution of Equation (11), these include the Mean Absolute Percentage Error (MAPE), computed as the absolute loss value of h over $\mathscr{T}_K$ in percentage

$$\mathrm{MAPE}(h) = \frac{100}{K} \sum_{i=1}^{K} \left| \frac{y_i^t - h(\boldsymbol{X}_i^t)}{y_i^t} \right|, \tag{12}$$

the Mean Absolute Error (MAE), computed as the absolute loss of h over $\mathscr{T}_K$

$$\mathrm{MAE}(h) = \frac{1}{K} \sum_{i=1}^{K} \left| y_i^t - h(\boldsymbol{X}_i^t) \right|, \tag{13}$$

and the Pearson Product-Moment Correlation Coefficient (PPMCC), which measures the linear dependency between $h(\boldsymbol{X}_i^t)$ and y_i^t with $i \in \{1, 2, ..., M\}$, given by

$$\mathrm{PPMCC}(h) = \frac{\sum_{i=1}^{K} \left(y_i^t - \bar{Y}\right) \left(h(\boldsymbol{X}_i^t) - \hat{\bar{Y}}\right)}{\sqrt{\sum_{i=1}^{K} \left(y_i^t - \bar{Y}\right)^2} \sqrt{\sum_{i=1}^{K} \left(h(\boldsymbol{X}_i^t) - \hat{\bar{Y}}\right)^2}} \tag{14}$$

where $\bar{Y} = \frac{1}{K} \sum_{i=1}^{K} y_i^t$ and $\hat{\bar{Y}} = \frac{1}{K} \sum_{i=1}^{K} h(\boldsymbol{X}_i)$. Other state-of-the-art error measures exist, but from a physical point of view, the ones already reported give a complete description of the quality of the model, therefore we only report these in Section 5.

4.4 Solution Method

Given the nature of the problem, a global Derivative-Free Optimisation (DFO) method must be utilised, as obtaining or estimating the derivatives of the physical models with respect to the parameters $\boldsymbol{\theta}$ is a computationally and time-intensive procedure. The literature on DFO methods is quite large, with a variety of algorithms that can solve a diverse class of problems [19].

We have employed Particle Swarm Optimisation (PSO) for a variety of reasons, including the reduced number of parameters to tune, constraints acceptance and speed in providing good solutions. Its stochastic properties allow for solution variability and thorough exploration of the search space in the initial iterations, with a local search behaviour during the final iterations. Finally, it is robust and well suited to handle non-linear, non-convex design spaces with discontinuities, and is readily available in most numerical platforms. Regarding the algorithm's parameters, we applied linearly decreasing inertia with a starting value of 1.15, and set the velocity of each particle to be influenced by a local neighbourhood of 90% of the entire swarm. Finally, for the velocity adjustment of each particle between iterations, the relative weighting of each particle's best position and the local neighbourhood's best position were both set to 1.5.

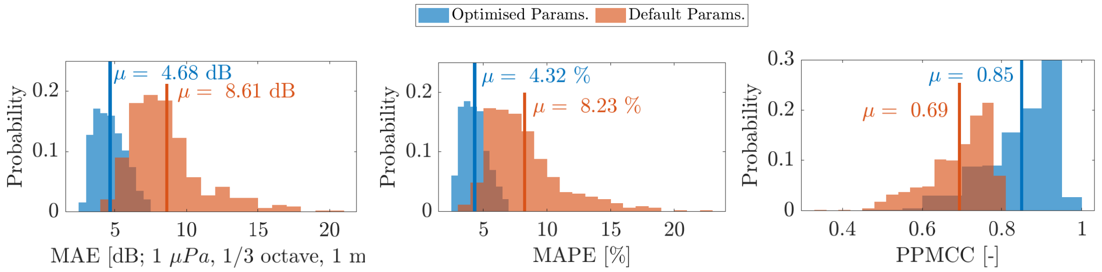

(a) MAE (b) MAPE (c) PPMCC

Figure 4: Histograms of performance metrics.

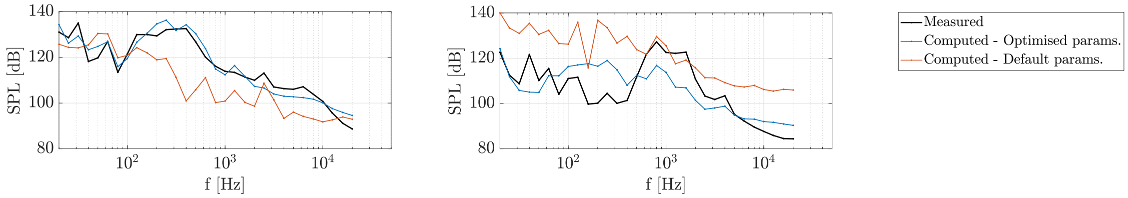

(a) Most accurate predictions. (b) Least accurate predictions.

Figure 5: Computational and experimental results on two different cases.

5 SIMULATION RESULTS

In Figure 4, we summarise the performance metrics on $\mathscr{T}_K$, for the parameter values optimised on $\mathscr{D}_N$, and the parameters reported in literature, as presented in Table 2. Overall, the optimised parameters present a remarkable performance improvement over the default values, with MAE $=$ 4.68 dB, MAPE $= 4.32\%$, and PPMCC $= 0.85$, whereas for the default parameters, the metrics are equal to 8.61dB, 8.23%, and 0.69 respectively. Considering the error distributions of Figure 4, it is clear that also the variance of all three metrics has decreased, indicating more robust and stable predictions. With the default parameter values, the MAE varies between 4.6 and 21 dB, the MAPE lies between 4.3% - 24%, and PPMC has a spread between 0.35 - 0.8. However, the optimised parameter values show consistently accurate predictions, with MAE varying between 2.8 and 7.5 dB, MAPE lying between 2.6% - 7%, and PPMC lying between 0.46 - 0.96.

We report comparative results between the measurements and computed URN spectra on two specific experiments in Figure 5. Figure 5(a) corresponds to the experiment for which computations and measurements show the highest agreement, and Figure 5(b) corresponds to the experiment with the highest discrepancy. It is clear that in both cases the default parameter values result in seemingly uncorrelated, with respect to the measured URN, predictions. However, the optimised parameter values show remarkable agreement for Figure 5(a), with a more plausible trend for Figure 5(b). Although not all experiments are presented for the sake of brevity, it suffices to state that the overall agreement lies between these two cases.

It is worth mentioning that the overall difference between the default and the optimised parameter values for the ETV model is limited, with deviations less than ±7%, in line with their physical interpretation. On the other hand, notable differences are observed for the parameters of the Matusiak model, which are worthy of attention due to their inherent physical meaning. More specifically, the parameter τ_c, which controls the number of oscillations for which bubble motion is simulated, has an optimal value of 350. Physically, this implies that bubble motion was simulated as long as possible, until the oscillations have been essentially dampened out. Furthermore, the fractal order m of the size distribution of the bubbles, which signified the complexity of the phenomenon [1], was also reduced from its initial value of 9, to the value of 2. Moreover, the gas / vapour fraction β was reduced to 0.15, and the parameter C, which controls the cavity thickness at the point of break-off, was increased to a value of 6 (from its initial value of 1.8), signifying the presence of larger bubbles. Finally, the number of bubble classes (N_c) also increased dramatically from its initial value (equal to 5) to the value of 500, which corresponds to the upper limit set during the optimisation process. This implies the requirement that each bubble be treated individually, or the use of a very fine discretization grid, to obtain accurate results.

It is interesting to note that similar results have also been reported in [18], in which the authors applied the same method to measurements taken from a container ship, which can be considered as a further validation of the results obtained in this work. However, it is worth noting that the simulation of bubble motion for a much higher number of oscillations than the one reported in [1], along with the finer discretization grid for the bubbles (by adjusting the parameter N_c), resulted in an increase in computation time by a factor of 12.

6 CONCLUSIONS

In this work, a methodology for the prediction of URN by a cavitating marine propeller has been presented and discussed. The methodology involves modelling and computational efforts that are compatible with the typical propeller / ship design process, making it suitable for design applications. The comparison between computations and experimental measurements indicates that the methodology employed is able to capture the most relevant aspects of the propellers' acoustic behaviour, despite a number of limitations associated with the assumptions taken. The combination of the ETV model, responsible for predicting noise due to a cavitating tip vortex, and the model of Matusiak for the broadband effects of sheet cavitation, can be a valuable tool for practical evaluation of propeller cavitation noise, showing good overall agreement with measurements. However, they are influenced by several empirical constants, the effects of which warrants further investigation.

Acknowledgements

The authors gratefully acknowledge that the research presented in this paper was carried out as part of the EU funded H2020 project, VENTuRE (grant no. 856887).

The authors would like to express their gratitude to Dr. Batuhan Aktas, who generated and kindly provided the experimental data used in the present work.

REFERENCES

[1] J. Matusiak. *Pressure and noise induced by a cavitating marine screw propeller*. PhD thesis, Aalto University, 1992.

[2] J. Bosschers. A semi-empirical prediction method for broadband hull-pressure fluctuations and underwater radiated noise by propeller tip vortex cavitation. *Journal of Marine Science*

and Engineering, 6(2):49, 2018.

[3] S. Gaggero and D. Villa. Cavitating propeller performance in inclined shaft conditions with openfoam: Pptc 2015 test case. *Journal of Marine Science and Application*, 17(1):1–20, 2018.

[4] L. Morino and C. Kuo. Subsonic potential aerodynamics for complex configurations: a general theory. *AIAA journal*, 12(2):191–197, 1974.

[5] C. Hsin. *Development and analysis of panel methods for propellers in unsteady flow.* PhD thesis, Massachusetts Institute of Technology, 1990.

[6] J.A. Geurst. *Linearized theory of two-dimensional cavity flows.* PhD thesis, Delft University of Technology, 1961.

[7] Timothy Leighton. *The acoustic bubble.* Academic press, 2012.

[8] F.R. Gilmore. The growth or collapse of a spherical bubble in a viscous compressible liquid. Technical report, California Institute of Technology, 1952.

[9] A.E. Raestad. Tip vortex index-an engineering approach to propeller noise prediction. *The Naval Architect*, 1996.

[10] P.G. Saffman. *Vortex dynamics.* Cambridge university press, 1992.

[11] F. Proctor, N. Ahmad, G. Switzer, and F. Limon Duparcmeur. Three-phased wake vortex decay. In *AIAA Atmospheric and Space Environments Conference*, 2010.

[12] S.D. Jessup. *An experimental investigation of viscous aspects of propeller blade flow.* PhD thesis, The Catholic University of America, 1989.

[13] Y.T. Shen, S. Gowing, and S. Jessup. Tip vortex cavitation inception scaling for high reynolds number applications. *Journal of Fluids Engineering*, 131(7), 2009.

[14] H.M. Fitzpatrick and M. Strasberg. Hydrodynamic sources of sound. In *First Symposium on Naval Hydrodynamics*, pages 241–280, 1956.

[15] B. Maines and R. Arndt. The case of the singing vortex. *Journal of Fluids Engineering*, 119:271–276, 1997.

[16] B. Aktas. *A systematic experimental approach to cavitation noise prediction of marine propellers.* PhD thesis, Newcastle University, 2017.

[17] A. Angelopoulos, P.A. Fitzsimmons, and A.Y. Odabasi. A semi-empirical method for propeller broad-band noise. Technical report, British Maritime Technology Limited, 1988.

[18] Frans Hendrik Lafeber, Johan Bosschers, and Erik van Wijngaarden. Computational and experimental prediction of propeller cavitation noise. In *OCEANS 2015*, pages 1–9, 2015.

[19] C.A. Floudas and P. Pardalos. *Encyclopedia of optimization.* Springer Science & Business Media, 2008.